

Modeling transitional plane Couette flow

Maher Lagha and Paul Manneville

Laboratoire d'Hydrodynamique (LadHyX),
CNRS-École Polytechnique, F-91128 Palaiseau, France.

Eur. Phys. J. B **58** (2007) 433–447.

Abstract

The Galerkin method is used to derive a realistic model of plane Couette flow in terms of partial differential equations governing the space-time dependence of the amplitude of a few cross-stream modes. Numerical simulations show that it reproduces the globally sub-critical behavior typical of this flow. In particular, the statistics of turbulent transients at decay from turbulent to laminar flow displays striking similarities with experimental findings.

PACS: 47.27.Cn, 47.60.+i

1 Introduction

The transition to turbulence in shear flows close to a solid wall is far from being completely understood. This situation arises because linear stability analysis is less fruitful for systems in which transient algebraic energy growth may become relevant than when exponentially growing modes are present [1]. It seems indeed easier to understand the case of super-critical instabilities (especially in closed-flow configurations such as Rayleigh–Bénard convection and the Taylor–Couette instability for which the classical tools of weakly nonlinear analysis are available) than the case of discontinuous transitions marked by a competition between solutions derived from linear theory and other fully nonlinear solutions. An interesting review of the main issues related to this problem can be found in [2]. A classical example of *globally sub-critical* transition is plane Poiseuille flow —the flow between two fixed

parallel plates driven by a pressure gradient— which is linearly unstable only beyond some high Reynolds number R_c [3] while *turbulent spots*, *i.e.* patches of turbulent flow scattered amidst laminar flow and separated from it by well defined fronts, can develop for R as low as about $R_c/4$ [4]. The situation is even worse for plane Couette flow (pCf in the following), the simple shear flow driven by two plates moving parallel to one another, which is stable for all R , *i.e.* $R_c = \infty$ [5], but experiences a direct transition to turbulence at moderate values of R [6, 7, 8, 9]. *Linear* theory, modal and non-modal [1], arguably indicates ways to escape from the laminar regime but is of limited help to understand the main problem alluded to above, namely the nature of the nontrivial *nonlinear* state and the coexistence in physical space of these different solutions.

Direct numerical simulations of the Navier–Stokes equations (DNS) have been intensively used to identify elementary processes involved in the sustenance of the nontrivial turbulent state, see *e.g.* [10]. An interesting approach was the reduction to a *minimal flow unit* (MFU) introduced by Jimenez and Moin [11], in which the dimensions of the simulation domain were decreased down to sizes for which turbulence is just maintained. The resulting dynamics can then be understood as a chaotic evolution of large coherent structures driving smaller eddies in a more or less stochastic way (though strict separation of scales is not legitimate). From observations of near-wall turbulent flow [10], Waleffe was able to derive a differential model involving the amplitude of a few modes associated to such coherent structures [12], in the spirit of a Galerkin approach that was made more systematic by Eckhardt and co-workers [13, 14, 15] using Fourier modes or by Holmes and co-workers [16] using empirical modes extracted from DNS by proper orthogonal decomposition.

Such models indeed help one to illustrate some of the mechanisms involved in the sustenance of turbulence or the competition between laminar and turbulent states in phase space. However, they are intrinsically and explicitly low-dimensional, which situates the problem within the context of discrete dynamical systems appropriate to *temporal* chaos, *e.g.* in discussing transients in terms of fractal border of the laminar-flow basin of attraction in phase space [17]. Therefore, they do not allow one to approach such problems as spot propagation that require full reference to the physical space. When similar questions were posed for convection, *i.e.* pattern formation and *spatio-temporal chaos*, it was found particularly valuable to pass from ordinary differential systems that can only deal with temporal behavior, such as the Lorenz model, to partial differential equations that also account for spatial dependence, *e.g.* the Swift–Hohenberg model [18] and its numerous variants. The present paper is devoted to the derivation and use of such a

closed set of partial differential equations appropriate to the pCf. This case is particularly interesting since, in contrast with other wall-bounded flows such as Poiseuille flow or the laminar boundary layer (Blasius) flow, it completely lacks linear instability and the absence of downstream advection makes it practical to observe the long term dynamics of spots, a crucial element of the sub-critical transition to turbulence.

Contrasting with the regime of developed turbulence taking place at large R , which requires a refined space-time resolution able to account for a cascade toward small scales, the transitional regime around R_g involves structures that appear to be coherent and large, i.e. occupy the full gap between the plates [19]. In turn, a model in terms of a few well-chosen modes with low wall-normal resolution should be sufficient for describing spots and understanding their dynamics. The amplitudes of these modes would then be taken as functions of the in-plane coordinates. This is the reason why we speak of *2.5-dimensional models*. In this terminology, the number 2 stands for the full in-plane space dependence (x, z) and the suffix .5 suggestively expresses that the dependence on the third, cross-stream, coordinate y is only partly taken into account through low order truncation. This strategy has been developed previously for easy-to-treat but unphysical *stress-free* boundary conditions at the plates bounding the flow [20] yielding interesting results but at unrealistically low Reynolds numbers [21, 22]. Here we focus on realistic *no-slip* boundary conditions. In the next section, we recall the primitive equations and give a hint on how the Galerkin method is developed. Next we turn to the explicit derivation of the model (the no-slip and stress-free models are compared at a formal level in §2.3). The numerical implementation is described in §3. Our main results are presented in Section 4, essentially bearing on the globally sub-critical character of the transition to turbulence (§4.1). The behavior of associated transients is then studied by experiments where the system is quenched from a turbulent state at large R towards ever decreasing values of R (§4.4). These results are discussed and some conclusions are drawn in Section 5.

2 The 2.5D models of 3D transitional flow

2.1 Primitive perturbation equations

The Navier-Stokes equation and continuity condition for an incompressible flow read:

$$\partial_t \mathbf{v} + \mathbf{v} \cdot \nabla \mathbf{v} = -\nabla p + \nu \nabla^2 \mathbf{v} + \mathbf{f}, \quad (1)$$

$$\nabla \cdot \mathbf{v} = 0, \quad (2)$$

where $\mathbf{v} \equiv (u, v, w)$, p is the pressure and ν is the kinematic viscosity. Further, ∇^2 denotes the three-dimensional Laplacian and the term \mathbf{f} accounts for a driving bulk force, if necessary.

Two types of boundary conditions can be considered, either the easy-to-handle but unrealistic stress-free (sf) conditions, or the natural and realistic no-slip (ns) conditions. In the sf case, the fluid is supposed to slip on the walls so that the flow has to be maintained by a fictitious bulk force $\mathbf{f} \propto \sin(\beta y/h)$ with $\beta = \pi/2$, further adjusted to produce the basic velocity profile $U_b^{\text{sf}}(y) = U_p \sin(\beta y/h)$. In contrast, with ns boundary conditions, the motion of the plates is able to drive the flow, which (when laminar) results in the linear velocity profile $U_b^{\text{ns}}(y) = U_p y/h$, where $2U_p$ is the relative speed of the plates, and $2h$ is the gap between them.

In the following we use dimensionless quantities. According to common usage, lengths and speeds are scaled with h , and U_p , respectively. In the ns case, the basic velocity profile thus reads $U_b^{\text{ns}} = y$ for $y \in [-1, 1]$, and the Reynolds number is $R = U_p h / \nu$. The models are further written for the perturbation (u', v', w', p') to the laminar basic flow that defines the $\hat{\mathbf{x}}$ direction, $\mathbf{v}_b = U_b \hat{\mathbf{x}}$, with $U_b = U_b^{\text{sf}}$ or U_b^{ns} , *i.e.* $u = U_b(y) + u'$, $v = v'$, $w = w'$, $p = p'$, so that (1,2) then read:

$$\begin{aligned} \partial_t u' + u' \partial_x u' + v' \partial_y u' + w' \partial_z u' \\ = -\partial_x p' - U_b \partial_x u' - v' \frac{d}{dy} U_b + R^{-1} \nabla^2 u', \end{aligned} \quad (3)$$

$$\begin{aligned} \partial_t v' + u' \partial_x v' + v' \partial_y v' + w' \partial_z v' \\ = -\partial_y p' - U_b \partial_x v' + R^{-1} \nabla^2 v', \end{aligned} \quad (4)$$

$$\begin{aligned} \partial_t w' + u' \partial_x w' + v' \partial_y w' + w' \partial_z w' \\ = -\partial_z p' - U_b \partial_x w' + R^{-1} \nabla^2 w', \end{aligned} \quad (5)$$

$$0 = \partial_x u' + \partial_y v' + \partial_z w'. \quad (6)$$

The Galerkin method is a special case of a *weighted residual method* [23]. It consists here in forcing the separation of in-plane and wall-normal coordinates by expanding the perturbations (u', v', w', p') onto a complete basis of y -dependent orthogonal functions satisfying the BCs with *amplitudes* dependent on (x, z, t) . The equations of motion are then projected onto the *same* functional basis, using the canonical scalar product. The main modeling step is then performed when truncating these expansions at a low order and keeping the corresponding number of residuals in order to get a consistent and closed system governing the amplitudes retained.

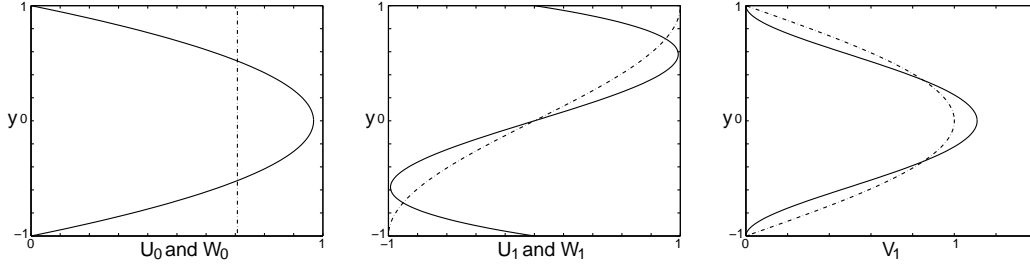


Figure 1: Profiles of the basis functions used for the perturbation to the base flow in the derivation of the ns model (solid lines), compared to their counterparts for the sf model (dashed-dotted lines) using the same mean-square normalization: drift flow $B(1 - y^2)$ vs. $1/\sqrt{2}$, first odd component $Cy(1 - y^2)$, vs. $\sin(\pi y/2)$, and first even component $A(1 - y^2)^2$ vs. $\cos(\pi y/2)$.

2.2 The no-slip model at lowest order

The free-slip model introduced in [20] and used more extensively in [22] was developed by taking advantage of the fact that trigonometric functions form a closed set under differentiation and multiplication. Perturbations were taken of the form: $v' = V_1 \cos(\beta y)$ and¹ $\{u', w'\} = \sqrt{1/2}\{U_0, W_0\} + \{U_1, W_1\} \sin(\beta y)$ with $\beta = \pi/2$ and the derivation of the model was straightforward. Numerical simulations have shown that it displays the expected globally sub-critical transition to turbulence but at unrealistically low Reynolds numbers [21]. This can be attributed to the underestimation of viscous dissipation effects implied by the choice of sf boundary conditions, in the same way as for convection where the sf threshold is about $2/5$ that for ns conditions ($27\pi^4/4$ vs. 1708). The derivation of a model for the realistic case by a similar Galerkin approach is harder because simple trigonometric expansions do not satisfy the simultaneous conditions:

$$v'(y = \pm 1) = \partial_y v'(y = \pm 1) = 0 \quad (7)$$

obtained by combining the continuity equation (6) with the conditions

$$u'(y = \pm 1) = w'(y = \pm 1) = 0. \quad (8)$$

To overcome this difficulty we take a basis consisting of polynomials in the wall-normal coordinate y , which also forms a family of functions closed under

¹Here the amplitude of the y -independent function is normalized differently than in [20, 22] in order to ease forthcoming comparisons.

multiplication and differentiation. A strict Galerkin approach is followed [24, Chap. 11, §10], with projections defined using the canonical scalar product:

$$\langle f, g \rangle = \int_{-1}^{+1} f(y)g(y) \, dy.$$

From conditions (7) it is clear that the expansion for v' must be taken of the form [25, p. 110]:

$$v' = (1 - y^2)^2 \sum_n V_{n+1} R_n(y) \quad (9)$$

where the $R_n(y)$, $n = 0, 1, \dots$ are polynomials of increasing degree n . The basis for u' and w' is then obtained by requiring that (6) be verified for each n and that the basis be orthonormal. It can be checked that these two conditions can be satisfied simultaneously and that u' and w' expands as

$$\{u', w'\} = (1 - y^2) \sum_n \{U_n, W_n\} S_n(y) \quad (10)$$

where the expression of $S_n(y)$ derives from that of $R_n(y)$ using the rules stated above. The Galerkin procedure isolates the dependence of the velocity field on the cross-stream coordinate y and, in expansions (9,10), U_m , V_m , W_m are just functions of the in-plane coordinates x , z , and time t .

It is quite simple to restrict consistently to the lowest possible order, *i.e.* keeping only functions associated to U_0 , W_0 , U_1 , V_1 , and W_1 as for the lowest order stress-free model. This is due to the parity properties of the functions involved that automatically guarantee the orthogonality of the different contributions to the velocity field. Our expansion will thus be based on

$$v' = V_1 A (1 - y^2)^2, \quad (11)$$

as the equivalent of $V_1 \cos(\beta y)$ and accordingly:

$$\{u', w'\} = \{U_0, W_0\} B (1 - y^2) + \{U_1, W_1\} C y (1 - y^2), \quad (12)$$

in replacement of $\frac{1}{\sqrt{2}}\{U_0, W_0\} + \{U_1, W_1\} \sin(\beta y)$. We need not worry about expanding the pressure since, at each stage of the Galerkin projection, pressure contributions —here P_0 and P_1 — introduce themselves as Lagrange multipliers serving to fulfill the successive projections of the continuity equation (6), here just the projections on the lowest order even and odd velocity basis functions (12). Physically, the contribution to the flow identified by (U_0, W_0) corresponds to the streak component induced by the lift-up mechanism acting through the component V_1 of the contribution (U_1, V_1, W_1) , a

part of which corresponds to streamwise vortices, flow structures that play an important role in the self-sustainment of wall-turbulence. Going beyond lowest consistent truncation order is tractable but somewhat tedious and we believe that the lowest order model contains all the large scale features present in the experiment at a qualitative level and can account for them at a semi-quantitative level.

Throughout the derivation, integrals to be computed are of the form:

$$J_{n,m} = \int_0^1 y^n (1 - y^2)^m dy = \sum_{k=0}^m \binom{k}{m} \frac{(-1)^k}{2k + n + 1},$$

where the $\binom{k}{m}$ are the binomial coefficients. For example, the normalization constants are given by: $A^2 = 1/2J_{0,4} = 315/256$, $B^2 = 1/2J_{0,2} = 15/16$, and $C^2 = 1/2J_{2,2} = 105/16$.

Amplitudes introduced in (11,12) are all functions of x , z , and t . The drift-flow component (U_0, W_0) now has a plane Poiseuille profile, in close correspondence with what happens in the Rayleigh-Bénard case, as first noticed by Siggia and Zippelius [26] and subsequently exploited to derive the generalized Swift-Hohenberg model described in [27]. Figure 1 compares the profiles of the basis functions for the free-slip and no-slip cases used at lowest consistency order.

According to the prescriptions of the Galerkin method, we insert the assumed expansions (11,12) in the continuity equation (6), then we multiply it by $B(1 - y^2)$ and integrate over the gap, which extracts its even part:

$$\partial_x U_0 + \partial_z W_0 = 0. \quad (13)$$

In the same way, multiplying (6) by $Cy(1 - y^2)$ and integrating extracts the odd part that reads:

$$\partial_x U_1 + \partial_z W_1 = \beta V_1, \quad (14)$$

where the quantity $\beta = \sqrt{3} = \beta^{\text{ns}}$ has the same order of magnitude as the one appearing in the stress-free model $\beta^{\text{sf}} = \pi/2$ (see §2.3).

Doing appropriate manipulations on (3) and (5), we obtain the even parts as

$$\begin{aligned} \partial_t U_0 + N_{U_0} &= -\partial_x P_0 - a_1 \partial_x U_1 - a_2 V_1 \\ &\quad + R^{-1} (\Delta - \gamma_0) U_0, \end{aligned} \quad (15)$$

$$\begin{aligned} \partial_t W_0 + N_{W_0} &= -\partial_z P_0 - a_1 \partial_x W_1 \\ &\quad + R^{-1} (\Delta - \gamma_0) W_0, \end{aligned} \quad (16)$$

with $a_1 = 1/\sqrt{7}$, $a_2 = \sqrt{27/28}$, $\gamma_0 = 5/2$, and

$$\begin{aligned} N_{U_0} &= \alpha_1(U_0\partial_x U_0 + W_0\partial_z U_0) \\ &\quad + \alpha_2(U_1\partial_x U_1 + W_1\partial_z U_1 + \beta'V_1U_1), \end{aligned} \quad (17)$$

$$\begin{aligned} N_{W_0} &= \alpha_1(U_0\partial_x W_0 + W_0\partial_z W_0) \\ &\quad + \alpha_2(U_1\partial_x W_1 + W_1\partial_z W_1 + \beta'V_1W_1), \end{aligned} \quad (18)$$

with $\alpha_1 = 3\sqrt{15}/14$, $\alpha_2 = \sqrt{15}/6$, $\beta' = 3\sqrt{3}/2 = \frac{3}{2}\beta$. In (15,16) and below Δ denotes the two-dimensional Laplacian $\partial_{xx} + \partial_{zz}$.

In the same way, the odd part of (3) and (5) read:

$$\begin{aligned} \partial_t U_1 + N_{U_1} &= -\partial_x P_1 - a_1\partial_x U_0 \\ &\quad + R^{-1}(\Delta - \gamma_1)U_1, \end{aligned} \quad (19)$$

$$\begin{aligned} \partial_t W_1 + N_{W_1} &= -\partial_z P_1 - a_1\partial_x W_0 \\ &\quad + R^{-1}(\Delta - \gamma_1)W_1, \end{aligned} \quad (20)$$

with $\gamma_1 = 21/2$ and

$$\begin{aligned} N_{U_1} &= \alpha_2(U_0\partial_x U_1 + U_1\partial_x U_0 \\ &\quad + W_0\partial_z U_1 + W_1\partial_z U_0 - \beta''V_1U_0), \end{aligned} \quad (21)$$

$$\begin{aligned} N_{W_1} &= \alpha_2(U_0\partial_x W_1 + U_1\partial_x W_0 \\ &\quad + W_0\partial_z W_1 + W_1\partial_z W_0 - \beta''V_1W_0), \end{aligned} \quad (22)$$

with $\beta'' = \sqrt{3}/2 = \frac{1}{2}\beta$.

Finally, the equation for V_1 is obtained in the same way by projecting (4) onto (11), which yields:

$$\partial_t V_1 + N_{V_1} = -\beta P_1 + R^{-1}(\Delta - \gamma'_1)V_1, \quad (23)$$

$$N_{V_1} = \alpha_3(U_0\partial_x V_1 + W_0\partial_z V_1), \quad (24)$$

with $\gamma'_1 = \beta^2$ and $\alpha_3 = 5\sqrt{15}/22$.

Notice that coefficients α_j behave as constants in the model, while the β s are analogous to wave-vectors accounting for cross-stream differentiation applied to the corresponding terms. In the same spirit one could remark that, in (15), $a_2 = \beta'a_1 = \frac{3}{2}\beta a_1$. Another point worth mentioning is that, by construction, the nonlinearities in the model preserves the energy conservation properties of the advection term $\mathbf{v} \cdot \nabla \mathbf{v}$. This fact is indeed important because the nonlinear evolution is formally governed by a quadratic expression which may produce singularities in a finite time. Energy conservation can be verified by computing the evolution of $E_t = E_0 + E_1 = \frac{1}{2}(U_0^2 + W_0^2) + \frac{1}{2}(U_1^2 + V_1^2 + W_1^2)$. This tedious task can be by-passed by taking advantage of the identity: $\mathbf{v} \cdot \nabla \mathbf{v} \equiv \nabla \left(\frac{1}{2} \mathbf{v}^2 \right) + \boldsymbol{\omega} \cdot \mathbf{v}$, with $\boldsymbol{\omega} = (\nabla \mathbf{v})^t - \nabla \mathbf{v}$, where $(\nabla \mathbf{v})^t$ is the transpose of tensor $\nabla \mathbf{v}$, which leads to the rewriting of the advection terms given in the appendix.

Table 1: Comparison of coefficients for the sf and ns models at lowest order. Definitions are those introduced for the no-slip model and further identified term-by-term in the stress-free model (the factors $\sqrt{2}$ all stem from the normalization convention for the y -independent mode associated to amplitudes $\{U_0, W_0\}$, see Figure 1 and the text relative to the sf basis).

coefficient	β	β'	β''	a_1	a_2
stress-free (sf)	$\pi/2$	β^{sf}	0	$1/\sqrt{2}$	$a_1^{\text{sf}}\beta^{\text{sf}}$
no-slip (ns)	$\sqrt{3}$	$\frac{3}{2}\beta^{\text{ns}}$	$\frac{1}{2}\beta^{\text{ns}}$	$1/\sqrt{7}$	$\frac{3}{2}a_1^{\text{ns}}\beta^{\text{ns}}$
sf/ns	0.907	0.605	0	1.871	1.131

coefficient	α_1	α_2	α_3	γ_0	γ_1	γ_1'
stress-free (sf)	$1/\sqrt{2}$	$1/\sqrt{2}$	$1/\sqrt{2}$	0	$(\beta^{\text{sf}})^2$	$(\beta^{\text{sf}})^2$
no-slip (ns)	$3\sqrt{15}/14$	$\sqrt{15}/6$	$5\sqrt{15}/22$	$5/2$	$21/2$	$(\beta^{\text{ns}})^2$
sf/ns	0.852	1.095	0.803	0	0.235	0.822

2.3 Comparison of stress-free and no-slip models

The no-slip model derived above appears to be slightly more general than the stress-free model initially presented in [20]. The two models have exactly the same structure, apart from the term multiplied by β'' which is absent in the stress-free case. Furthermore, when normalized in the same way, their coefficients are comparable, while the main difference lies, as expected, in the terms associated to viscous dissipation. Let us examine Table 1 in detail.

As already said, values found for the quantity β in (14), which measures the typical order of magnitude of gradients in the wall-normal direction, are close to each other since $\beta^{\text{ns}} = \sqrt{3} \approx 1.732$ and $\beta^{\text{sf}} = \pi/2 \approx 1.571$.

Coefficients $a_{1,2}$ and α_{1-5} appearing in the other equations are also not very different in the two models. From the sf/ns entries in the table, one can see that ratios are all within a factor less than two, with the exception of β'' which is zero in the stress-free case owing to the special relations existing between trigonometric lines. As far as non-normal effects and nonlinear interactions are concerned, one may think that the two models are close to each other and that the dynamics that they generate will be robust (the effects of the differences could be studied in detail by considering fictitious alternate models with arbitrary coefficients, i.e. not derived from any systematic

Galerkin approach).

The most important difference between the two models shows up in the expression of the viscous terms. Whereas in the stress-free model, the drift velocity component $\{U_0, W_0\}$ can relax only through in-plane modulations *via* the terms involving Δ , an additional damping is observed in the no-slip case with coefficient $5/2$ in (15,16) independent of the in-plane dependence of that flow component. In the same way the damping of components $\{U_1, W_1\}$ is much stronger in the no-slip case with coefficient $\gamma_1 = 21/2$ in (19,20), than in the stress-free case with coefficient $(\pi/2)^2 \approx 2.41$. The ns wall-normal viscous timescale is thus four times shorter than the sf one. Accordingly, if turbulence can be sustained in the stress-free model at some value R , already independently of other sources of damping and while the mechanisms are expected to retain most of their intensity as discussed in the previous paragraph, a similar situation is expected for about $4R$ in the no-slip model. Of course the argument is very rough but it shows that one goes in the right direction since the stress-free model is known to underestimate thresholds by a large factor [21].

Another important feature of the no-slip model is that an (x, z) -independent component of U_1 can be created as the flow evolves, so that the model already contains a mean flow correction to the base profile $U_b(y) = y$ even when truncated at lowest order. In contrast, a similar correction formally appears only at a much higher order in the stress-free model, as pointed out in [15]. In the latter case, velocity profiles attached to U_1 and W_1 are indeed the same as that of the base flow and accordingly do not modify its shape though an equivalent mean contribution also exists. This feature is further examined in the next subsection.

2.4 Mean flow correction

Let us consider the average value

$$\mathcal{D}^{-1} \int_{\mathcal{D}} U_1(x, z, t) dx dz \equiv \overline{U}_1(t)$$

of the streamwise perturbation velocity component U_1 over the domain \mathcal{D} at the boundary of which perturbations cancel, or else periodic boundary conditions apply. The equation governing $\overline{U}_1(t)$ is easily obtained by averaging (19) over the domain. On its right hand side, the only term that remains in the average is the one that is not the gradient of some quantity, i.e. $-\gamma_1 R^{-1} \overline{U}_1$, accounting for viscous dissipation. The evaluation of $\int_{\mathcal{D}} N_{U_1} dx dz$ leads to $\overline{N}_{U_1} = \alpha_2(\beta + \beta'') \mathcal{D}^{-1} \int_{\mathcal{D}} U_0 V_1 dx dz$. This quantity —the space-independent contribution to the streamwise component of the Reynolds

stress— is easily obtained after some simple algebra using the continuity conditions (13,14). Gathering the results we get the evolution equation for the mean flow correction as:

$$\frac{d}{dt}\overline{U}_1 = \alpha_2(\beta + \beta'')\overline{U}_0\overline{V}_1 - \gamma_1 R^{-1}\overline{U}_1. \quad (25)$$

As will be illustrated later (cf. Figure 4), a fully turbulent regime at steady state will display a time-independent non-zero—in fact negative— correction, arising from the compensation of the two terms on the right hand side.

The spanwise component of the correction \overline{W}_1 is governed by the same equation as (25) provided that we make the general change $U \mapsto W$. However \overline{W}_1 is expected to cancel on average for a turbulent regime at steady state as a consequence of the $z \mapsto -z$ symmetry of the original problem. The full set of perturbation equations is indeed symmetric in the interchanges $x \leftrightarrow z$ and $U \leftrightarrow W$ except for the presence of the term $-a_2 V_1$ accounting for lift-up in (15), which has no equivalent in its spanwise analogue (16). This is the only term that singles out the streamwise direction, subsequently introducing the difference between \overline{U}_1 and \overline{W}_1 . A non-zero \overline{W}_1 could then only result from an instability breaking that symmetry.²

Whereas it is clear that no such correction exists for V_1 since \overline{V}_1 obviously cancels all the time (no net flux across the layer for impermeable walls), we must also consider averaging the fields U_0 , W_0 . The equation for \overline{U}_0 reads:

$$\frac{d}{dt}\overline{U}_0 = \alpha_2(\beta - \beta')\overline{U}_1\overline{V}_1 - \gamma_0 R^{-1}\overline{U}_0. \quad (26)$$

A similar equation can be obtained for \overline{W}_0 through the change $U \mapsto W$. The source terms for \overline{U}_0 and \overline{W}_0 are however expected to be small since, from the continuity condition (14), U_1 and W_1 are spatially out of phase with V_1 . These terms can even be expected to cancel statistically since otherwise they would generate net contributions to the transfer of momentum in the x and z directions and correlative finite dissipation terms $-\frac{5}{2}R^{-1}\overline{U}_0$ and $-\frac{5}{2}R^{-1}\overline{W}_0$. As long as the global symmetries of the problem are not broken, net fluxes \overline{U}_0 and \overline{W}_0 are forbidden by the general $x \mapsto -x$ and $z \mapsto -z$ symmetries in the same way as $\overline{W}_1 \neq 0$ is forbidden by the $z \mapsto -z$ symmetry (in contrast with \overline{U}_1 which has its own source term).

It can be noticed that, in the stress-free case, mode ‘0’ has no source term for accidental reasons linked to trigonometric relations between base functions (i.e. $\beta = \beta'$). Furthermore, that mode has no cross-stream dependence so that it cannot be ironed out by viscous dissipation. Accordingly, \overline{U}_0 and

²Such a symmetry breaking was experimentally observed in the upper part of the transitional regime of pCf [28], a range of Reynolds numbers which is out of reach of our present modeling due to its reduced cross-flow resolution.

\overline{W}_0 retain their initial values which, in turn, can freely be set to zero due to the in-plane Galilean invariance specific to stress-free boundary conditions.

3 Numerical implementation

The equations derived above have been implemented on domains of various streamwise and spanwise sizes L_x and L_z with periodic boundary conditions, which allowed us to develop a standard Fourier pseudo-spectral numerical scheme [29]. The diagonal viscous terms were integrated in spectral space exactly. The nonlinear advective terms and the non-normal terms arising from linearization around the base flow were evaluated in physical space and integrated in time using a second order Adams–Bashforth scheme also used to treat the average velocity components $\overline{U}_j, \overline{W}_j$, $j = 0, 1$. Fast Fourier transforms were used to pass from spectral to physical space and *vice versa*. Convergence of the results was checked by taking different time steps δt and space steps $\delta x, \delta z$. In the range of Reynolds numbers under consideration, $\delta t = 0.01$ and $\delta x = \delta z = 0.25$ were found appropriate and used throughout the study.

Simulations were performed in boxes with sizes ranging from $\mathcal{D} = L_x \times L_z = 8 \times 8$ up to 64×64 , although the model was originally designed for wide domains. A few short control runs were performed for \mathcal{D} up to 128×128 . At any rate, results presented here are mostly dedicated to checking that the no-slip model captures the essential features of the globally sub-critical nature of the transition to turbulence in pCf, as a prerequisite to future work. In fact, the sizes considered here are already several times larger than the expected streak spacing $\lambda_z \sim 6$ [19]. In the terms of chaos theory, we would speak of “weak confinement” (see [25, Chap. 8] and below §4.2) in contrast with “strong confinement” legitimating the reduction to low dimensional differential systems.

Obtained with limited computing power, simulation results presented here have already their own interest as will be shown in §4.4 but let us emphasize the fact that accepting low cross-stream resolution was the price to be paid for enlarging the domains up to sizes that are much larger than what can be dealt with in direct simulations with highly resolved cross-stream dependence.³

Two further points are worth mentioning about the implementation of the

³In their study of the relaxation of oblique turbulent bands observed in the experiments [28], Barkley and Tuckerman [30] performed direct simulations in a quasi-one-dimensional box making an angle with the streamwise direction, very long in the direction perpendicular to the bands but a few MFUs long in the direction parallel to them, which represents an intermediate stage.

model. First, the continuity conditions (13,14) are dealt with by introducing appropriate stream functions Ψ_0 , Ψ_1 and velocity potentials Φ_1 such that:

$$U_0 = \overline{U}_0 - \partial_z \Psi_0, \quad W_0 = \overline{W}_0 + \partial_x \Psi_0, \quad (27)$$

and

$$U_1 = \overline{U}_1 + \partial_x \Phi_1 - \partial_z \Psi_1, \quad W_1 = \overline{W}_1 + \partial_z \Phi_1 + \partial_x \Psi_1, \quad (28)$$

with

$$\beta V_1 = \Delta \Phi_1. \quad (29)$$

Though not necessary on general grounds, the introduction of the additional quantities \overline{U}_0 , \overline{W}_0 , \overline{U}_1 , and \overline{W}_1 , is forced by our choice of in-plane periodic boundary conditions for the fields Ψ_0 , Ψ_1 , and Φ_1 . This is because these uniform components are generated by contributions to the potential Φ_1 and stream-functions Ψ_0 , Ψ_1 that would vary linearly with x and z , a spatial dependence that is precluded by their representations as Fourier series expansions inherent in our computational approach.

The velocity contributions derived from these equations are next reintroduced in the expression of the nonlinearities when needed. The equations governing Ψ_0 and Ψ_1 are obtained by cross-differentiating and subtracting the equations for the velocity components in the usual way. Taking the divergence of these equations yields an equation for the pressure which is next used to determine the potential part of the velocity field accounted for by Φ_1 . The main advantage of introducing the fields Ψ_0 , Ψ_1 , and Φ_1 is that one can construct arbitrary but physically relevant divergence free velocity fields as initial conditions since this characteristic is built in their definitions. The uniform corrections $(\overline{U}_1, \overline{U}_0, \overline{W}_1, \overline{W}_0)$ are computed in parallel by integrating (25,26) and their W counterparts. The equations that have been numerically implemented are gathered in the appendix.

4 Results

4.1 Global sub-criticality

Global sub-criticality of the model is depicted in Figure 2 which displays the behavior of the mean perturbation energy *per* unit surface as a function of the Reynolds number R . A discontinuous transition can indeed be observed around $R_g \approx 175$. Whether R_g represents a real threshold (called *global stability* threshold in previous studies, hence the subscript ‘g’) or just marks some crossover is presently a debated topic for plane Couette flow [31, 32] as well as for Poiseuille flow in a circular pipe which is also a linearly stable

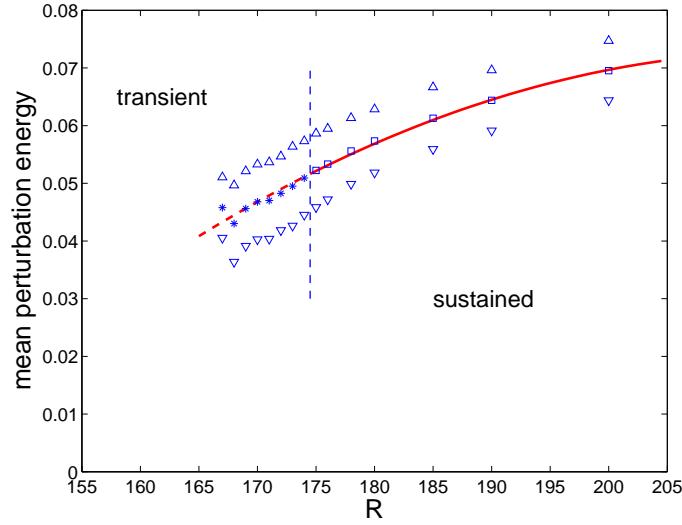


Figure 2: Variation of the mean perturbation energy *per* unit surface with R . Evidence of a global stability threshold $R_g \approx 175$. Values corresponding to squares $R > R_g$ correspond to sustained regimes, those corresponding to transients are marked with asterisks. Up and down triangles indicate the root-mean-square amplitudes of instantaneous fluctuations around the corresponding means. The computational domain is $\mathcal{D} \equiv 32 \times 32$.

flow that becomes turbulent under finite amplitude perturbations [32, 33, 34]. For $R > R_g$ spontaneous collapse of the uniformly turbulent state was not observed, even when pursuing the simulation for very long durations. For example, at $R = 175$ the turbulent state persisted over more than 3×10^5 time units.⁴ On the other hand, below ≈ 174.5 , the laminar state was systematically obtained but at the end of turbulent transients that could be of variable lengths. This result was obtained by combining *quench* experiments in which a state prepared at $R = R_i = 200$ was allowed to evolve after R had been suddenly decreased to some lower value R_f and *adiabatic* experiments where R was varied by small increments and the initial state at the new lower value of R was taken as the final state of the experiment at the previous value. The persistent turbulent regime at $R = 175$ was obtained in this second way, which —according to us— indicates a lower stability bound for the turbulent state at least over the corresponding time interval and for the considered size ($L_x = L_z = 32$) since the procedure minimizes the perturbation brought to

⁴For experiments in water with a gap $2h = 7\text{mm}$, in the transitional range, $R \sim 315$, the time unit (turnover time h/U_p) is $3.8 \times 10^{-2}\text{s}$, so that the time length $\sim 3 \times 10^5$ would correspond to about 3 hours, much longer than what could be done in the laboratory under sufficiently well controlled conditions [35].

the flow, especially regarding its uniform component \overline{U}_1 . In contrast, above R_g the initial finite perturbation brought to the system in quench experiments may be sufficient to make it leave the attraction basin of the turbulent state and return to the laminar state. Indeed, if the turbulent regime is a genuine attractor, its attraction basin shrinks to zero as R approaches R_g from above and, with it, the size of the perturbation brought to the turbulent state necessary to make it decay toward the laminar state, in particular that linked to the fact that \overline{U}_1 is not at equilibrium for the new value of R after the quench. At any rate, it appears that the range of interest for the transition is no longer as low as in the sf case but approaches the experimental value [35].

A series of transients obtained in quench experiments from $R_i = 200$ to $R_f = 171$ is illustrated in Figure 3. It can be seen that they end quite abruptly so that it makes sense to define a conditional mean perturbation energy restricted to the plateau value, before final decay.⁵ Such conditional averages are indicated as asterisks in Figure 2 while squares denote averages corresponding to sustained turbulent regimes. The line through the data points is a fit against a parabolic expression that has no theoretical foundation but strongly suggests that it goes smoothly through the critical value R_g . In particular, taking the mean perturbation energy as an order parameter, we find no evidence of the proximity of a turning-point bifurcation as was tentatively suggested in earlier studies from analogies with elementary bifurcation theory [35].

The amplitudes of the fluctuations of the average perturbation energy (conditional for transient states) are indicated by the up and down triangles in Figure 2 and, again, no remarkable behavior (i.e. divergence) can be noticed around $R \sim R_g$. As discussed in the next sub-section, their amplitude is comparatively large only because, in this study, the size of the domain \mathcal{D} has been chosen relatively small. The detailed statistics of the transients' lifetimes, which is the main original result presented in this paper, is studied in §4.4.

4.2 Extensivity of the sustained turbulent regime

It has been argued elsewhere by one of us (PM in [2]) that the modeling in terms of low-dimensional ordinary differential systems [12] may give valuable hints only about the mechanisms of turbulence sustenance well beyond the transitional regime but not necessarily about the transitional regime itself,

⁵A similar observation was made by Faisst & Eckhardt [36] in numerical simulations of Poiseuille pipe flow. They pointed out that it was not possible to distinguish between sustained turbulence and turbulent transients before decay.

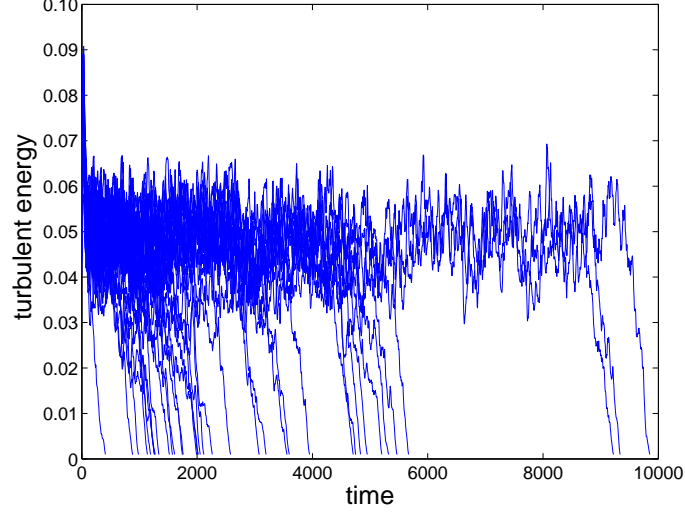


Figure 3: Total perturbation energy *per* unit surface E_{tot} as a function of time in a series of transients from a turbulent flow prepared at $R_i = 200$ suddenly quenched at $R_f = 171 < R_g \approx 175$.

Table 2: Perturbation energy *per* unit surface: time average and fluctuations for $R = 200$.

$\mathcal{D} : L_x \times L_z$	16×16	32×16	32×32	64×32
$\langle E_{\text{tot}} \rangle$	0.06935	0.06932	0.06956	0.06980
$\sigma_{E_{\text{tot}}} (\times 10^3)$	10.33	7.21	5.58	3.62
$\frac{\sqrt{L_x L_z} \sigma_{E_{\text{tot}}}^{L_x L_z}}{16 \sigma_{E_{\text{tot}}}^{16 \times 16}}$	1.0	0.987	1.079	0.992

$\mathcal{D} : L_x \times L_z$	64×64	128×64	128×128
$\langle E_{\text{tot}} \rangle$	0.06965	0.06959	0.06948
$\sigma_{E_{\text{tot}}} (\times 10^3)$	2.61	1.758	1.179
$\frac{\sqrt{L_x L_z} \sigma_{E_{\text{tot}}}^{L_x L_z}}{16 \sigma_{E_{\text{tot}}}^{16 \times 16}}$	1.010	0.9629	0.9132

where spatio-temporal behavior is involved. Indeed, the main underlying hypothesis of this kind of modeling is that the space-time dependence of the perturbations can be described by mixing a small number of modes with frozen space dependence and time varying amplitudes. Specific resonances between modes make the temporal properties of the system, notably the fractal properties associated to chaotic transients, excessively sensitive to the physical size of the equivalent confined system. Furthermore, the approach is intrinsically unable to deal with the growth or decay of turbulence through the coexistence of laminar and turbulent domains that fluctuate in space and time [40]. When considering this specific problem, it seems legitimate to require that, to be appropriate, a model should display some kind of statistical robustness when the size of the simulation domain is varied [38]. An indication that our model behaves appropriately in the turbulent regime is obtained by considering the total perturbation energy *per* unit surface and its fluctuations as the surface of the simulation domain is increased. Table 2 displays our results. A series of experiments over domains $\mathcal{D} = L_x \times L_z$ was performed, with domain surfaces multiplied by factors $n = 1, 2, \dots, 64$, starting from $\mathcal{D} = 8 \times 8$ and for $R = 200$.

For the smallest systems considered, turbulence was only transient at $R = 200$. Needing larger R to get sustained turbulence is not surprising since much dissipation is associated with the in-plane space dependence forced by periodic boundary conditions at short distances, which raises the thresholds for complex behavior. For $\mathcal{D} = 8 \times 8$, the domain can only fit a very small number of structures so that the transient is better analysed in terms of chaotic saddles in the context of *temporal chaos* [39]. For $\mathcal{D} = 16 \times 8$ turbulence is again transient but the dynamics has a more spatio-temporal flavor than for 8×8 , hence closer to what is obtained at larger sizes. Evidence that the turbulent regime at $R = 200$ is *extensive* for larger domains, in practice beyond $\mathcal{D} = 16 \times 16$, is obtained from the facts that (i) the time average of E_{tot} is independent of the size and (ii) the fluctuations around this average value decrease roughly as the inverse square root of the size.

The extensivity property is valid for the uniformly turbulent regime but size effects may still be expected to affect the transition process, especially in view of the presence of large scale flows resulting from the space modulation of the mean flow correction to be discussed in the next sub-section, as soon as strong inhomogeneities are present. This study only suggests us a typical size below which the temporal approach is better suited.

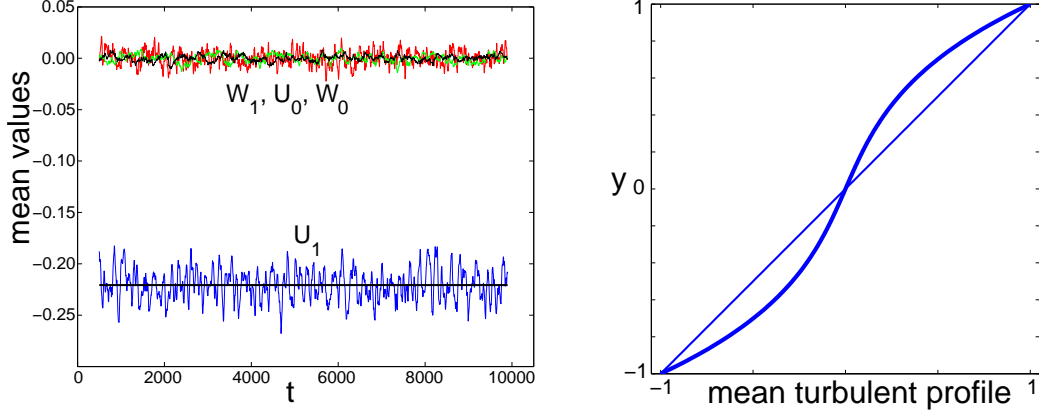


Figure 4: Correction to the base flow for a sustained turbulent regime obtained as described in the text ($R = 200$, $\mathcal{D} = 32 \times 32$). Top panel: Traces of the average flow components \overline{U}_1 , \overline{W}_1 , \overline{U}_0 , and \overline{W}_0 as functions of time. Bottom panel: Mean turbulent flow profile $u_{\text{mf}} = y + \overline{U}_1 C y (1 - y^2)$, the value of \overline{U}_1 is obtained by averaging the above relevant trace over $t \in [0.5, 15] \times 10^3$.

4.3 Mean flow in the sustained turbulent regime

An important feature of our model is that it already contains corrections to the base flow at the lowest truncation order. Figure 4 illustrates the result of a specially designed experiment at $R = 200$ starting from an initial condition taken from some fully turbulent state, in which all the components of mode ‘1’ were artificially turned off. During a brief transient that has been cut off, the streamwise contribution to the mean flow \overline{U}_1 builds up. As seen in the figure, it is negative and statistically constant, with time average $\langle \overline{U}_1 \rangle_t = -0.221$ and standard deviation $\Sigma_{\overline{U}_1} = 0.015$. In contrast, the transverse contribution averages to zero: $\langle \overline{W}_1 \rangle_t = 1.4 \times 10^{-4}$ with $\Sigma_{\overline{W}_1} = 6.9 \times 10^{-3}$ ($\approx 50 \langle \overline{W}_1 \rangle_t$ for the specific numerical simulation considered). At the same time, \overline{U}_0 and \overline{W}_0 also average to zero: $\langle \overline{U}_0 \rangle_t = -2.4 \times 10^{-4}$, $\Sigma_{\overline{U}_0} = 3.3 \times 10^{-3}$ and $\overline{W}_0 = -1.5 \times 10^{-5}$, $\Sigma_{\overline{W}_0} = 2.9 \times 10^{-3}$. The mean turbulent flow profile is displayed in Figure 4 (bottom) as the superposition of a correction $C y (1 - y)$ with amplitude \overline{U}_1 to the base flow $U_b = y$, pointing out the expected formation of a central region with reduced shear. It will be interesting to study the patches of negative U_1 that appear during the growth/decay of turbulent spots [37], as a local counter-part to the steady state uniform correction in the sustained turbulent regime.

4.4 Transients below the global stability threshold

The global stability threshold R_g is best defined as the value of the control parameter below which the nontrivial state, here the turbulent regime, is unstable and thus cannot be sustained in the long term. Accordingly the trivial state, here the laminar flow, is the only possible equilibrium solution, whatever the initial configuration (or accidental perturbations). Many studies have been devoted to the transition from laminar *to* turbulent flow, either under the effect of natural fluctuations, upon triggering specific localized perturbations, or upon modifying the base flow in a well-controlled way (see the review in [21]). In such experiments, the turbulent state may be reached with finite probability only due to the local stability of the base flow, which explains the dispersion of results in early studies and some sensitivity to the triggering process. In contrast, from the very definition of R_g , it may seem less ambiguous to start *from* the turbulent side at large Reynolds numbers and study its relaxation as R is decreased. As already mentioned one can consider either an *adiabatic* decrease of R which minimizes the risk of introducing dangerous perturbations, or else *quench* experiments using the same methodology as the one which produced the experimental value $R_g \approx 325$ [19]. The cumulative distribution of transient lifetimes was then studied and found to display an exponential tail of the form $\Pi(\tau' > \tau) \propto \exp(-\tau/\tau_R)$, where $\Pi(\tau' > \tau)$ is the probability of observing a transient with length τ' larger than some given time τ . In this expression τ_R is the characteristic decay time of the distribution. If it was effectively exponential from the start, then τ_R would be the mean transient length at the corresponding value of R . From that estimate, it was proposed that τ_R diverges to infinity as R approached R_g from below as

$$\langle \tau_{\text{tr}} \rangle \sim (R_g - R)^{-1}, \quad (30)$$

see [35, 31]. This behavior was recently questioned and a reexamination of the data lead to the proposal of an indefinite exponential increase [32] though the time scale computed in note 4 leaves little hope to check the extrapolation at larger R experimentally. Our quench experiments with the ns model is a tentative contribution to the debate.

Experiments were performed by quenching the system from series of uniformly turbulent states at $R = R_i = 200$. These states were obtained from snapshots taken during a single long experiment and sufficiently separated in time to be considered as independent turbulent initial conditions. The Reynolds number was next suddenly decreased to a final value $R = R_f$. In order to be able to perform statistics over a large number of independent trials, we took a domain size \mathcal{D} that was reduced as much as possible, though

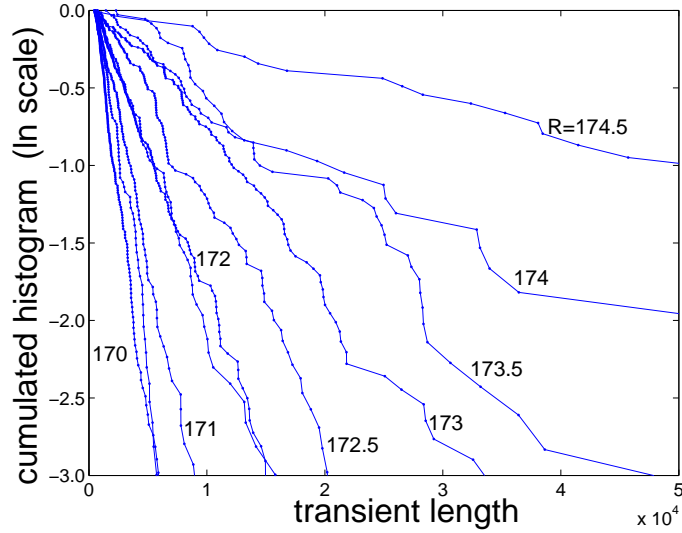


Figure 5: Distribution of transient lifetimes in quench experiments with $R_i = 200$ and variable R_f in semi-log plot.

sufficiently large to preserve the extensivity property of the uniformly turbulent regime. $\mathcal{D} = 32 \times 32$ was chosen but runs with $\mathcal{D} = 128 \times 32$ or 128×64 were performed for purposes of control or pattern imaging (see §4.5).

The lifetimes of individual transients were determined as the times needed to reach some cut-off value of the total perturbation energy *per* unit surface E_t below which the system immediately and irreversibly decays to the laminar state, as can easily seen in Figure 3 displaying a typical set of experiments to be analysed. The statistics were checked to be insensitive to the precise value chosen for the cut-off provided that it was sufficiently below 0.015. Here the cut-off was uniformly taken equal to 0.0015 (see also later, Fig. 10). The very late stage of decay for $E_{\text{tot}} < 0.0015$ appears to correspond to a fast exponential viscous damping of streaks.

Below $R = 175$, transients with variable lifetimes began to appear and well-defined lifetime distributions were seen to develop, while relaxation could be considered as “immediate” below $R = R_u \approx 164$ (notation introduced in [35]). Upon approaching $R_g \approx 175$ from below, using lin-log scales Figure 5 shows that the statistics of transient lifetimes are indeed exponentially decreasing and that the slope decreases as R_f increases.

The slopes of the exponential tails were determined by fitting them with straight lines. The result is plotted in Figure 6 as open dots, either in linear scale (top) or semi-log scale (bottom). If the distribution were exponential

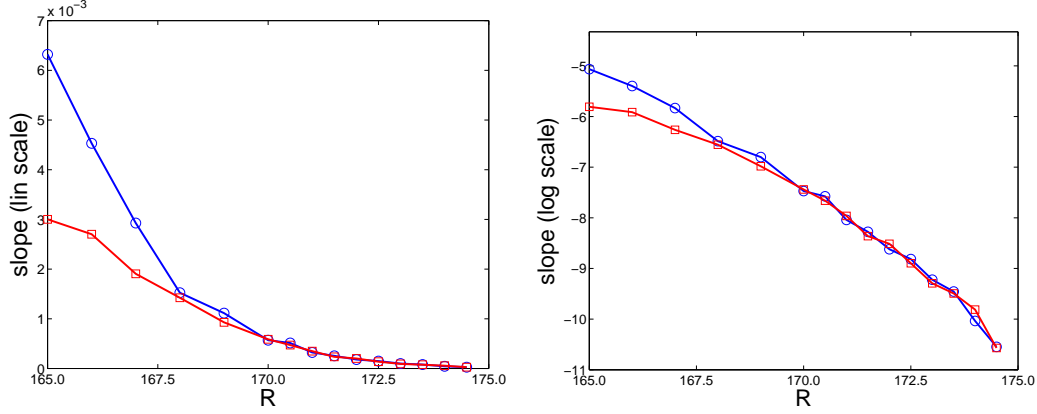


Figure 6: Slope of histogram tails in lin-log scale (Fig. 5) as a function of R . Top: lin-lin. Bottom: lin-(natural)log scale. Open dots: slope of histogram tails in semi-log plot; open squares: inverse mean length of transients computed as indicated in the text.

from the start, up to some offset value τ_{\min} , the slope would be given by $1/\langle\tau - \tau_{\min}\rangle$ where $\langle\ldots\rangle$ is the arithmetic mean over the observed transient lengths τ . Corresponding results are plotted as open squares in Fig. 6. Both estimates compare well with each other down to $R \sim 169$ below which they diverge. In fact, histograms for $R < 170$ were not presented in Fig. 5 in order not to overcrowd it with curves that would have needed another scale to make them discernable. These histograms display a shoulder corresponding to an accumulation of short transients that biases the computation of the slope from the inverse mean and explains the discrepancy between the two estimates. Conversely this assures us that the fit to an exponential is indeed satisfactory for $R \geq 170$.

It is, however, hard to put error bars on our results because we have a finite number of transients at our disposal, usually between 100 and 200 except for $R = 174$ and 174.5 for which we have only about 30 transients. To understand the origin of the difficulties, one must consider how the histograms evolve as the number of experiments increases. For example, the presence of a small number of measurements that seem atypical of the statistical tail implies an increase of the number of experiments by a large factor to rub out their effect. All the values plotted in Figure 6 are what we consider to be our *best estimates* based on careful inspection of individual histograms and comparisons of statistics obtained by including or excluding transient lengths that might be judged atypical of the overall decay behavior. In general all results were consistent to within less than 10%, especially at the largest values

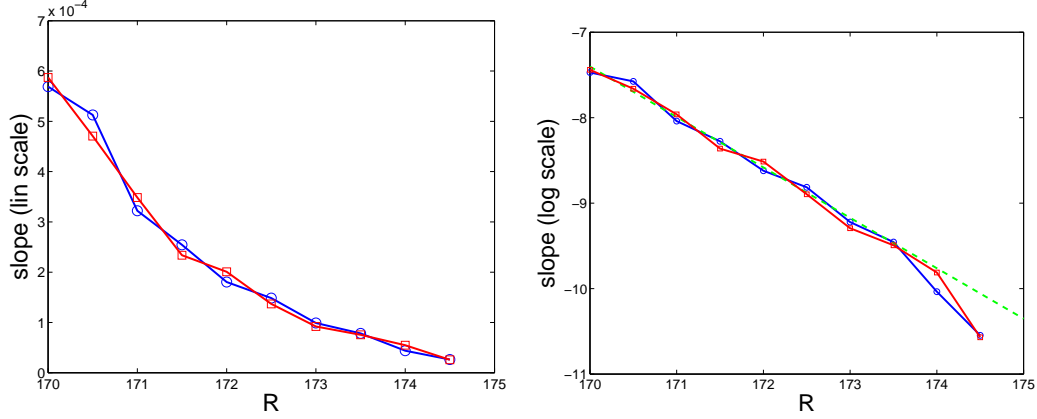


Figure 7: Slope histogram tails in lin-log scale as a function of R . Enlargement of Fig. 6. Top: lin-lin scale. Bottom: lin-(natural)log scale; the added dashed line is a guide for the eyes, showing the deviation of the top highest points from the overall exponential behavior. Symbols as in Fig. 6.

of R considered.

This being said, the zoom on the variation of the slope as a function of R displayed in Figure 7 confirms the exponential decrease of the terminal slope of histograms, or conversely an exponential increase of the characteristic decay time. However, the values corresponding to the points at $R = 174$ and 174.5 seem somewhat too small for them to stay aligned with the other points, as suggested by the dashed line in Figure 7 (bottom). This line is obtained from a linear fit of the logarithms of the slopes measured for $R \in [170, 173.5]$, which we consider as our most reliable estimates. The deviation can have two explanations:

- either, as discussed earlier, it is an artifact of our estimation procedure with an insufficient number of points but it turns out that the corresponding distributions were surprisingly regular and the slope estimation unambiguous,
- or it is a real effect indicating that the characteristic time increases faster than expected, i.e. diverges for some finite R_g that should be close to 175 (for which the turbulent attractor was found to be stable).

For $R = 174$ and 174.5 , an over-representation of long transients among our 30 or so samples would indeed explain the observed under-evaluation of the slope, which might be the trace of a genuine (turbulent) attractor for slightly larger values of R . Note also that the difference between the estimates obtained by slope fitting and by inverse means at $R = 174$ —quite anomalous

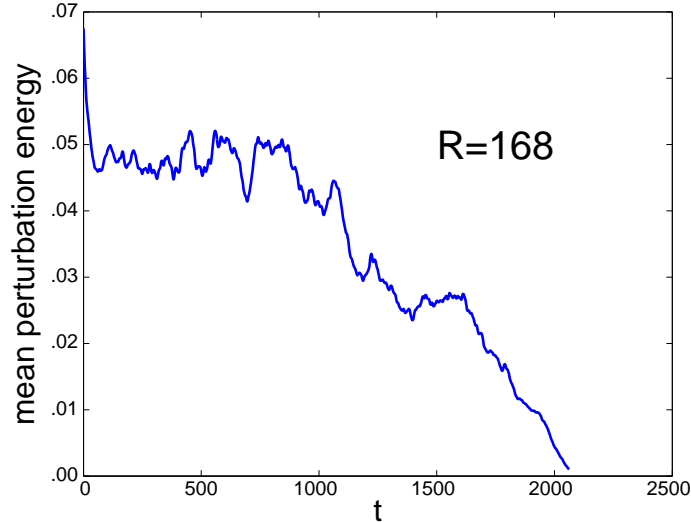


Figure 8: Mean perturbation energy as a function of time during a transient in a quench experiment at $R = R_f = 168$ starting from $R_i = 200$ for $L_x = 128$, $L_z = 64$.

in view of the general agreement between the two estimates when $R \geq 170$ —is entirely accounted for by the accidental absence of a sufficiently short transient τ_{\min} . Accordingly, we do not exclude the possibility of a crossover between the exponential regime typical of transients tentatively attributed to a chaotic saddle and a real divergence at some well defined R_g above which a turbulent attractor does exist. This divergence would be typical of a crisis converting the chaotic repeller into an attractor. The anomalously long transients observed for $R = 174$ and 174.5 would then be representative of the behavior just below the crisis point.

Finite size effects, still sizable at $\mathcal{D} = 32 \times 32$, will make it difficult to decide what is the actual behavior but we believe that considering larger systems, which is presently in progress, will help us to obtain a clearer picture of the transition. The next section is thus devoted to an illustration of a transient in a system of intermediate size with the purpose of showing that one cannot avoid the spatio-temporal feature of the dynamics in the transitional range of Reynolds numbers.

4.5 Illustration of decay during a transient at $R = 168$

In this subsection we consider a typical transient obtained for $R = 168$ with $L_x = 128$, $L_z = 64$, starting from $R = R_i = 200$. Figure 8 displays the

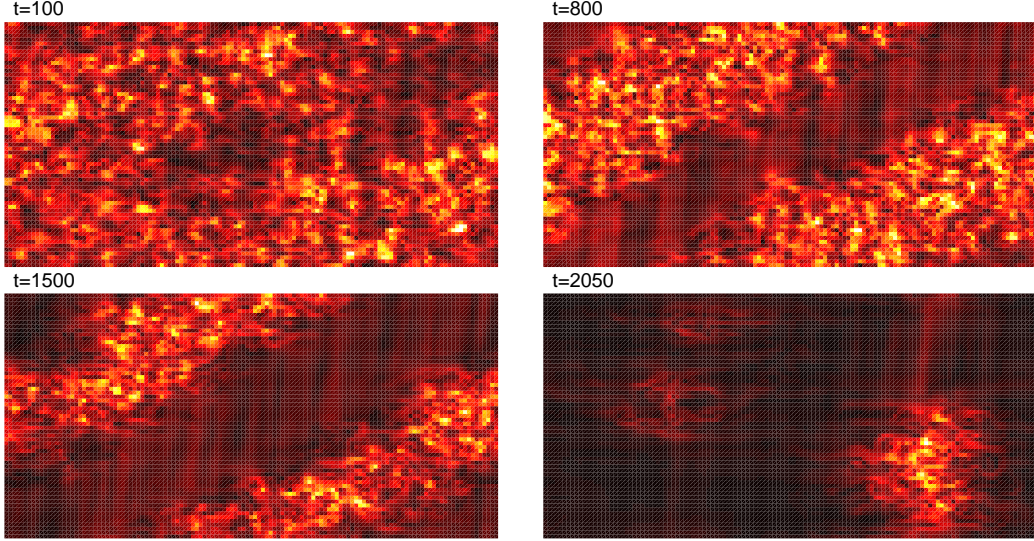


Figure 9: Four snapshots taken during a transient in a domain $\mathcal{D} = 128 \times 64$. Dark/deep red (clear/light yellow) regions correspond to small (large) perturbation speed [colored version on line]. One point out of 4 in each direction is represented, hence $\Delta x = \Delta z = 1$. The horizontal axis corresponds to the streamwise direction. The contribution of streaks to the perturbation is clearly visible at the laminar/turbulent frontier.

evolution of the mean perturbation energy as a function of time throughout the transient. The general aspect of this curve is similar to those in Figure 3, with a distinct plateau followed by an irreversible decay. Here, the transient is not very long since R_f is not close enough to R_g . Snapshots of the local perturbation velocity amplitude $\bar{u}(x, z, t)$ are given in figure 9. This quantity is defined as $\bar{u}(x, z, t) = \sqrt{2(E_0(x, z, t) + E_1(x, z, t))}$, where $E_0 = \frac{1}{2}(U_0^2 + W_0^2)$ is the local kinetic energy contained in the streaks and $E_1 = \frac{1}{2}(U_1^2 + V_1^2 + W_1^2)$ the kinetic energy contained in the remaining part of the departure from the laminar profile, including the contribution of streamwise vortices. This definition is reminiscent of that of a turbulent velocity intensity except that the latter is defined with respect to the mean flow. Here, this would have led us to subtract \bar{U}_1 , but would no longer have made sense for the spatially inhomogeneous turbulent regime during decay, as illustrated below.

Figure 9 presents several snapshots of the perturbation flow pattern at different key instants. First for $t = 100$, just after the quench, turbulence initially prepared at $R_i = 200$ gets stabilized at the level corresponding to $R_f = 168$. Though it is relatively uniform, one can already detect some large scale inhomogeneity. Later, this inhomogeneity increases up to a point

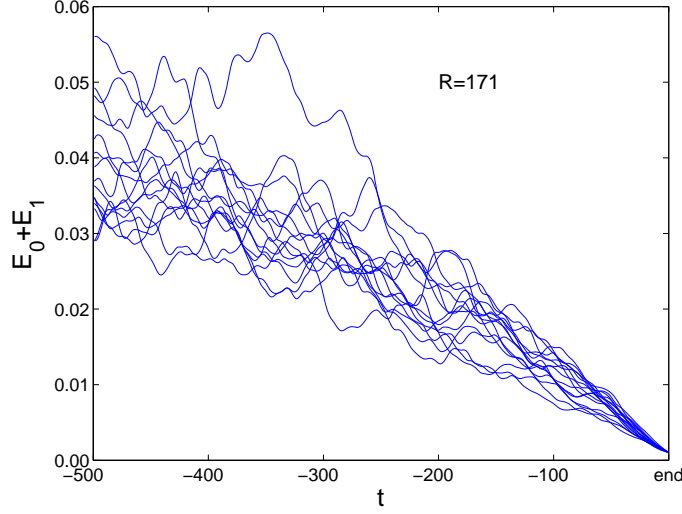


Figure 10: Variation of the total perturbation energy during the end of 15 of the transients in Fig. 3.

when oblique bands are conspicuous, as in the second image at $t = 800$ while the level of perturbation energy has remained essentially the same. Subsequently, the turbulent region becomes narrower and the perturbation energy decreases accordingly. At $t = 1500$, E_t is about the half of the initial energy content. The regular regression of the band ends when it breaks into several parts forming smaller patches that, in turn, decay as seen here for $t = 2000$. The regular regression of the width of the turbulent bands explains the roughly linear decrease of the mean perturbation energy for $T > 1000$ in Fig. 8 assuming that the front between the turbulent and laminar domains moves at constant speed.

In fact, a similar behavior was probably exhibited by transients already for $\mathcal{D} = 32 \times 32$ though the picture in physical space is less clear. Indirect evidence can be obtained by zooming on the last 500 times units of each transient. Figure 10 displays a superposition of 15 of them for $R = 171$ taken from the series used for Fig. 3. Statistically speaking, they all follow the same roughly linear decay, from the end of the plateau to the cut-off corresponding to the beginning of the final exponential viscous damping (not represented). Accordingly, and comparing to what happens for $\mathcal{D} = 128 \times 64$, it seems that we have a nucleation problem with a probability distribution for laminar germs of different sizes so that when a wide enough germ appears, the energy plateau ends and the turbulent domain recedes regularly. (At this stage, it could be noticed that uniformly subtracting about 500 time units

from the transient lengths would not change the overall statistical behavior.) The intensity of the mechanism sustaining turbulence, a function of R , is certainly essential in controlling this probability. Such a mechanism is sometimes studied using low dimensional dynamical systems modeling [12, 14, 16]. Accordingly, a way to reconcile this picture with that of chaotic saddles could be recovered but it is still not clear how to reintroduce physical space and correlative size effects. At any rate, considering a larger system will certainly shed light on this nucleation probability problem.

It is worth to mention that, during the decay and even at rather late stages, the energy remains much concentrated in the turbulent patches. It was empirically found that setting the cut-off between turbulent and laminar flow at $\bar{u} = 0.5\bar{u}_{\text{ref}}$, where \bar{u}_{ref} is the mean of \bar{u} in the starting reference state at $t = 100$, well discriminates the two regimes from each other. For example, at $t = 2000$, one finds that about 70% of the remaining energy is concentrated in 10% of the total surface. Going backwards in time, one gets that, at $t = 1500$, the turbulent band occupies about 48% of the surface and contains around 90% of the energy, and still earlier, that for $t = 800$, the turbulent fraction is about 87% and contains 98% of the energy.

To conclude this section, it should be remarked that the oblique band observed in Fig. 9 has no connection with the oblique turbulent bands experimentally observed in the upper transitional range [28] and numerically reproduced by Barkley and Tuckerman [30]. Here, its presence is clearly linked to the periodic boundary used and its development directly follows from the oblique ovoid shape of the inhomogeneity already present at the very beginning of the quench experiment. Depending on the size and average orientation of this inhomogeneity, the ultimate shape of the turbulent domain is either a longitudinal, a transverse, or an oblique band. In view of the size of modulations at $t = 100$ (Fig. 9, top), we think that a system at least four times as large as that used for this illustration should be considered in order to have a chance to explore several inhomogeneity patterns before decay. This is what motivates the simulations over a domain $\mathcal{D} = 256 \times 128$ presently in progress and alluded to above.

5 Conclusion

In this paper we have considered the low- R range of transitional pCf. On the one hand, modeling this situation in terms of low dimensional deterministic dynamical systems is limited due to the inherently spatiotemporal character of the problem. For example, decay from the sustained turbulent state close to the global stability threshold R_g is not well described as a chaotic

transient close to a crisis bifurcation point, even though exponential distributions of transient lifetimes are observed near this point [15], because this concept introduced in nonlinear dynamics is not adapted to the account of decay through regression of turbulent patches fluctuating in time and space. On the other hand, the direct connection to statistical physics suggested by Pomeau [40] and underlying the abstract spatio-temporal intermittency approach [41] may seem far-off though it takes spatial extension into account in an analogous way. Extending previous work by one of us [20, 22], the approach developed here intends to bridge the gap between low and high dimensional systems in a concrete way and with a semi-quantitative ambition.

Except for the fact that it fell short of predicting reasonable values of the transitional Reynolds numbers, the early stress-free attempt already contained many interesting features and its deficiency could easily be attributed to the use of unrealistic boundary conditions in the derivation of the model. The first part of the present paper was thus devoted to the derivation of a similar model, but appropriate to the physically realistic no-slip boundaries [24, 25, 27]. When truncated at the lowest significant order (§2.2), this new model was seen to have nonlinear and non-normal structures close to those of the stress-free model but with slightly different coefficients when basis functions used in the Galerkin expansion were appropriately normalized. The major differences, discussed in §2.3, appeared to be *(i)* the presence of an additional damping of the drift flow that was no longer cross-stream independent but had a more generic parabolic profile, *(ii)* a strongly enhanced viscous dissipation of the other flow components (associated to steeper variations of the Galerkin basis functions close to the plates), and *(iii)* the existence of a non-trivial mean correction to the base flow \overline{U}_1 already at lowest truncation order. As could be expected from the structural similarity of the models, the same qualitative behavior was obtained but a wide step in the right direction was made since the study presented in the second part of the paper showed that transitional Reynolds numbers of interest were now less than a factor of two off the experimental range, instead of a factor for ten with the stress-free model.

Experiments reported in [19, 42] clearly showed that, in the low- R part of the bifurcation diagram, the dynamics is dominated by processes involving flow structures that are coherent over the full gap between the plates and this is certainly the reason why the results obtained from the model are reasonably satisfactory. Increased dissipation associated to more resolved cross-stream dependence is expected to improve the agreement at the price of much more analytical and computational work already around R_g .

On the other hand, increasing the order of the model would certainly be necessary much beyond R_g , in particular in the range where the transition

‘oblique turbulent bands \leftrightarrow featureless turbulence’ takes place [30]. This is however not advisable since the model would then get more and more cumbersome explicit nonlinear terms from the Galerkin expansion which, in turn, would be truncated at increasingly insufficient orders, while it is clearly more economical to use a high precision pseudo-spectral scheme in the cross-stream direction.

Besides the observation that fully developed spatiotemporal chaos is extensive (§4.2), the main concrete result presented here relates to the determination of a possible global stability threshold R_g and the statistical behavior of transients close to R_g for systems of moderate size. As in laboratory experiments, a discontinuous transition was observed (§4.1, Fig. 2). Turbulent transients accounting for the relaxation of turbulence during quench experiments were shown to exhibit exponentially distributed lifetimes (§4.4, Fig. 5). Beyond $R \simeq 175$ the turbulent state was observed over time intervals that could seemingly be arbitrarily long, hence suggesting $R_g = 175$. For $R < 175$, the slopes of the exponential tails of the lifetime distributions were seen to approach zero exponentially as R increased, with a possible crossover to a diverging behavior close to the supposed R_g , in spite of post-processing uncertainties (Fig. 7).

Extending this conclusion to the case of transitional pipe Poiseuille flow [32, 33, 34] needs additional investigation before tentatively establishing any connection. Such a connection, which should be taken with care, has been made from a reanalysis of the pCf results that also leads to indefinite exponential decay with R of the slopes of histograms’ tails. In our opinion, in the Couette case available experimental data were however obtained for values of R somewhat too far from the hypothesized $R_g \simeq 325$ (determined from several independent ways) for supporting the conjecture of an underlying chaotic saddle typical of temporal chaos, especially in view of experimental pictures [35]. On the contrary, in close correspondence with these pictures, the illustration given in §4.5 clearly points to spatio-temporal chaos as explaining the transient behavior, with the statistical possibility of a local breakdown of the turbulent state, further extending to the whole system. This behavior is reminiscent of what happens at a thermodynamic phase change [40]. The size of the system for which these preliminary results have been obtained, $\mathcal{D} = 32 \times 32$, though situating it apparently inside the extensive regime, is clearly insufficient to probe any thermodynamic-like property of the transition, and *a fortiori* any issue related to universality in the sense of critical phenomena in statistical physics. We expect that the study currently in progress for $\mathcal{D} = 256 \times 128$, a size unreachable by direct numerical simulations, will bring us interesting results.

Since it represents a simplified version of the Navier–Stokes equations

at least for R not too large, our model can serve to study other questions posed by the transition to turbulence in globally sub-critical flows. For example, whereas it is clear how streamwise vortices generate streaks through the *lift up* mechanism introduced long ago, instability mechanisms and some processes involved in the regeneration of vortices are still unclear in spite of recent progress [2]. The very coexistence of laminar and turbulent flow implied by global sub-criticality, the mechanisms by which one of the phases gains against the other, i.e. how spots grow (*laminar* \rightarrow *turbulent* transition) or how the turbulent state recedes (*turbulent* \rightarrow *laminar* transition), how asymmetric these problems are, what is the role of the base flow modification inside a turbulent domain (local counter-part to §4.3 in the presence of large scale modulations), are questions that we intend to examine, with the stimulating perspective of going beyond the case of pCf and considering other wall flows of less academic interest but experiencing a similar transition to turbulence.

Appendix: Equations used in simulations

The equations for Ψ_0 , Ψ_1 , and Φ_1 that have been effectively implemented read:

$$\begin{aligned}
& \left[\partial_t - R^{-1} (\Delta - \gamma_0) \right] \Psi_0 \\
& \quad = \Delta^{-1} (\partial_z N_{U_0} - \partial_x N_{W_0}) + a_1 \left(\frac{3}{2} \partial_z \Phi_1 - \partial_x \Psi_1 \right) , \\
& \left[\partial_t - R^{-1} (\Delta - \gamma_1) \right] \Psi_1 \\
& \quad = \Delta^{-1} (\partial_z N_{U_1} - \partial_x N_{W_1}) - a_1 \partial_x \Psi_0 , \\
& \left[\partial_t - R^{-1} (\Delta - \beta^2)^{-1} (\Delta^2 - 2\beta^2 \Delta + \gamma_1 \beta^2) \right] \Phi_1 \\
& \quad = (\Delta - \beta^2)^{-1} \left[\Delta^{-1} \beta^2 (\partial_x N_{U_1} + \partial_z N_{W_1}) - \beta N_{V_1} \right] ,
\end{aligned}$$

where $\beta = \beta^{\text{ns}} = \sqrt{3}$ everywhere and the expressions of the advection terms have been rewritten in the energy conserving form mentioned in the text:

$$\begin{aligned}
N_{U_0} &= M_{U_0} + \partial_x E_a , \\
N_{W_0} &= M_{W_0} + \partial_z E_a , \\
N_{U_1} &= M_{U_1} + \partial_x E_b , \\
N_{W_1} &= M_{W_1} + \partial_z E_b , \\
N_{V_1} &= M_{V_1} + \beta E_b ,
\end{aligned}$$

where the “weighted” energies read:

$$\begin{aligned} E_a &= \frac{1}{2}\alpha_1(U_0^2 + W_0^2) + \frac{1}{2}\alpha_2(U_1^2 + W_1^2) + \frac{1}{2}\alpha_3V_1^2, \\ E_b &= \alpha_2(U_0U_1 + W_0W_1), \end{aligned}$$

and

$$\begin{aligned} M_{U_0} &= V_1(\alpha_2\beta'U_1 - \alpha_3\partial_xV_1) + \alpha_1W_0(\partial_zU_0 - \partial_xW_0) \\ &\quad + \alpha_2W_1(\partial_zU_1 - \partial_xW_1), \\ M_{W_0} &= \alpha_1U_0(\partial_xW_0 - \partial_zU_0) + \alpha_2U_1(\partial_xW_1 - \partial_zU_1) \\ &\quad + V_1(\alpha_2\beta'W_1 - \alpha_3\partial_zV_1), \\ M_{U_1} &= \alpha_2[W_0(\partial_zU_1 - \partial_xW_1) + W_1(\partial_zU_0 - \partial_xW_0)] \\ &\quad - \alpha_2\beta''V_1U_0, \\ M_{W_1} &= \alpha_2[U_0(\partial_xW_1 - \partial_zU_1) + U_1(\partial_xW_0 - \partial_zU_0)] \\ &\quad - \alpha_2\beta''V_1W_0, \\ M_{V_1} &= U_0(\alpha_3\partial_xV_1 - \alpha_2\beta U_1) \\ &\quad + W_0(\alpha_3\partial_zV_1 - \alpha_2\beta W_1). \end{aligned}$$

Velocity components are given by (27–29).

The evolution is computed in Fourier space by a numerical scheme that treats linear terms exactly and nonlinear terms by an Adams–Bashforth formula. Formally writing the evolution problem as

$$\frac{d}{dt}X = \mathcal{L}X + \mathcal{N}(X)$$

it can be seen that, in order to keep second order accuracy, we have to compute

$$\begin{aligned} X(t + \delta t) &= \exp(\mathcal{L}\delta t) \times \\ &\quad [X(t) + \delta t(1.5\mathcal{N}(X(t)) - 0.5\exp(\mathcal{L}\delta t)\mathcal{N}(X(t - \delta t)))]. \end{aligned}$$

When integrating the equations, it can also be verified that their r.h.s. cancel exactly at wave-vector $(k_x, k_z) = (0, 0)$ so that taking the inverse of Δ is a legitimate operation. As stated in the main text, average velocity components must be treated separately. Corresponding formulas for $(\overline{U}_1, \overline{U}_0)$ are obtained from (25,26) and those for $(\overline{W}_1, \overline{W}_0)$ by two similar equations with U replaced by W .

Acknowledgments

The authors acknowledge discussions with J.-M. Chomaz, C. Cossu, and P. Huerre at LadHyX, B. Eckhardt and J. Schumacher at Philipps Universität,

Marburg. P.M. specially thanks S. Bottin, O. Dauchot, F. Daviaud, and A. Prigent at Saclay for their past and present collaboration. L. Tuckerman and D. Barkley are thanked for interesting discussions and the communication of their own papers related to the problem treated here. The two anonymous referees are also deeply acknowledged for their thoughtful and constructive remarks that helped us to improve the manuscript.

Computations at $L_x = 128$, $L_z = 64$ were performed at IDRIS (Orsay) under project # 61462.

References

- [1] P. Schmid, D.S. Henningson, *Stability and transition in shear flows* (Springer, 2001).
- [2] T. Mullin & R. Kerswell, eds. *IUTAM Symposium on Laminar-Turbulent Transition and Finite Amplitude Solutions* (Springer, 2005).
- [3] S.A. Orszag, J. Fluid Mech. **50** (1971) 689–703.
- [4] D.R. Carlson, S.E. Widnall, M.F. Peeters, J. Fluid Mech. **121** (1982) 487–505.
- [5] V.A. Romanov, Anal. Ego. Prilo. **7**, (1973) 62–73.
- [6] A. Lundbladh, A. Johansson, J. Fluid Mech. **229** (1991) 499–516.
- [7] N. Tillmark, P.H. Alfredsson, J. Fluid Mech. **235** (1992) 89–102.
- [8] O. Dauchot, F. Daviaud, Europhys. Lett. **28** (1994) 225–230.
- [9] A. Prigent and O. Dauchot, “Transition *to* versus *from* turbulence in subcritical Couette flows” in [2], p. 195–219.
- [10] J.M. Hamilton, J. Kim, F. Waleffe, J. Fluid Mech. **287** (1995) 317–348.
- [11] J. Jiménez, P. Moin, J. Fluid Mech. **225** (1991) 213–240.
- [12] F. Waleffe, Phys. Fluids **9**, (1997) 883–900.
- [13] A. Schmieg, B. Eckhardt, Phys. Rev. Lett. **79** (1997) 5250–5253.
- [14] B. Eckhardt, A. Mersmann, Phys. Rev. E. **60** (1999) 509–517.
- [15] J. Moehlis, H. Faisst, B. Eckhardt, New Journal of Physics **6** (2004) 56–17.
- [16] T.R. Smith, J. Moehlis, Ph. Holmes, J. Fluid Mech. **528** (2005) 71–110.
- [17] B. Eckhardt, H. Faisst, “Dynamical systems and the transition to turbulence”, in [2], p. 35–50.

- [18] J. Swift, P.C. Hohenberg, Phys. Rev. A **15** (1977) 319–328.
- [19] S. Bottin, O. Dauchot, F. Daviaud, P. Manneville, Phys. Fluids **10** (1998) 2597–2607.
- [20] P. Manneville, F. Locher, C.R. Acad. Sci. Paris **328** Serie IIb (2000) 159–164.
- [21] P. Manneville, O. Dauchot, “Patterning and transition to turbulence in subcritical systems: the case of plane Couette flow,” in *Coherent structures in classical systems*, D. Reguera, L.L. Bonilla & J.M. Rubi, eds. (Springer, 2001).
- [22] P. Manneville, Theor. and Comp. Fluid Dyn. **18** (2004) 169–181.
- [23] B.A. Finlayson, *The method of weighted residuals and variational principles, with application in fluid mechanics, heat and mass transfer* (Academic Press, 1972).
- [24] P. Glansdorff, I. Prigogine, *Structure, Stabilité et Fluctuations* (Masson, 1971).
- [25] P. Manneville, *Dissipative structures and weak turbulence* (Academic Press, 1990).
- [26] E.D. Siggia, A. Zippelius, Phys. Rev. Lett. **47** (1981) 835–838.
- [27] P. Manneville, in *Cellular Structures in Instabilities*, J.E. Wesfreid & S. Zaleski, eds. Lect. Notes in Physics **210** (1983) 137–155.
- [28] A. Prigent, G. Grégoire, H. Chaté, O. Dauchot, W. van Saarloos, Phys. Rev. Lett. **89** (2002) 014501.
- [29] D. Gottlieb & S.A. Orszag, *Numerical analysis of spectral methods: theory and applications* (SIAM, 1977).
- [30] D. Barkley, L.S. Tuckerman, Phys. Rev. Lett. **94** (2005) 014502.
- [31] S. Bottin & H. Chaté, Eur. Phys. J. B **6** (1998) 143–155.
- [32] B. Hof, J. Westerweel, T.M. Schneider, B. Eckhardt, Nature **443** (2006) 59–62.
- [33] J. Peixinho & T. Mullin, Phys. Rev. Lett. **96** (2006) 094501.
- [34] A.P. Willis, R.R. Kerswell, Phys. Rev. Lett. **98** (2007) 014501.
- [35] S. Bottin, F. Daviaud, P. Manneville, O. Dauchot, Europhys. Lett. **43** (1998) 171–176.
- [36] H. Faisst, B. Eckhardt, J. Fluid Mech. **504** (2004) 343–352.
- [37] M. Lagha, P. Manneville, “Large scale flow around turbulent spots,” to appear in Phys. Fluids, 2007.

- [38] Y. Pomeau, C.R. Acad. sc. Paris **300** srie II (1985) 239–241.
- [39] B. Eckhardt & T.M. Schneider, “Edge states in the transition to turbulence in pipe flow”, EFM6 Stockholm, June 26-30, 2006.
- [40] Y. Pomeau, Physica D **23** (1986) 3–11.
- [41] H. Chaté, P. Manneville, “Spatiotemporal intermittency,” in *Turbulence, a tentative dictionary*, P. Tabeling & O. Cardoso, eds. (Plenum, 1995).
- [42] O. Kitoh, K. Nakabyashi, F. Nishimura, J. Fluid Mech. **539** (2005) 199–227.